A Perturbation Model for Imaging in Dense Scattering Media: Derivation and Evaluation of Imaging Operators

H. L. Graber[1], J. Chang[2,4], R. Aronson[3], R. L. Barbour[1,2]

SUNY Health Science Center at Brooklyn, 450 Clarkson Ave., Brooklyn, NY, 11203,
Departments of [1]Physiology and Biophysics, and [2]Pathology.

Polytechnic University, 333 Jay Street, Brooklyn, NY, 11201,
[3]Physics and [4]Electrical Engineering Departments.

1. INTRODUCTION

Most imaging schemes involve characterizing the interaction of an electromagnetic wave with a target medium. This interaction can be generally described by the wave equation:

$$\nabla^2\psi = \frac{1}{c^2}\frac{\partial^2\psi}{\partial t^2}. \qquad (1)$$

This equation relates the spatial variation (Laplacian) of the field to the electrical permittivity, ε, and magnetic permeability, μ, of the medium. The latter quantities account for the induced alignment of the electrical dipole (polarization) and magnetic moment (magnetization) in the material by the propagating field, and they determine c, the speed of light, which is equal to $1/\sqrt{\varepsilon\mu}$. For a time-harmonic source, equation 1 reduces to the Helmholtz equation:

$$\nabla^2\psi + k^2\psi = 0, \qquad (2)$$

where k, the wave number, is equal to ω/c, and ω is the wave frequency in radians-s^{-1}.

Measurement of the phase and amplitude of the electric field at a boundary is typically accomplished with an antenna or similar device. As the scattering cross-section of the material increases, the number of scattered fields combining with the incident field at a point on the surface grows rapidly. Because these fields arrive from points at different distances, their phase relationships with the incident field and with each other are certain to be randomly distributed [1]. Inversion of the wave equation in these circumstances is very difficult, if possible at all. It thus becomes necessary to employ an alternative theoretical framework in which knowledge of the wave properties of a scattered field is not necessary, but in which it may still be possible to acquire the needed information for image recovery from measurements of only the energy of the field. This alternative framework is provided by using the radiation transport equation (RTE) instead of the wave equation for deducing the effect of a dense scattering medium on an incident radiation field [1]. The RTE is formally identical to the Boltzmann

Published in: *Medical Optical Tomography: Functional Imaging and Monitoring*
(SPIE Institutes Vol. IS11, SPIE Optical Engineering Press, 1993)

equation used in neutron transport theory [2], and its use implies that radiation is being treated as a particle phenomenon, with scattering being reinterpreted as the deflection of light particles (photons) from their initial paths by collisions with structures in the medium, rather than as diffraction of waves. To be consistent with this framework, the energy of light, rather than the wave properties of its electromagnetic field, must be the property that is measured.

Since our first suggestion in 1988 [3,4], our group has explored the application of perturbation-based image recovery schemes derived from the RTE [5-9]. Our global interest in this area originated from an appreciation that development of practical schemes could serve to greatly extend the range of imaging applications. This follows because such development would permit the use of energy sources previously considered unsuitable and could allow for the examination of media to greater depths or having greater thickness than were previously feasible.

2. MEASUREMENT SCHEMES

In many antenna applications, and other situations requiring measurement of electromagnetic fields, plane wave illumination is frequently used [10,11]. This type of illumination scheme, however, would not be the most advantageous when analyzing the scattered field using approaches derived from the RTE. The reason for this is that as the area of illumination increases, the photons received by a detector after passing through a given point becomes a smaller fraction of the total number detected, thereby reducing the sensitivity of the detector to localized inhomogeneities. What is required instead is an illumination and detection scheme that maximizes the ability to discern localized inhomogeneities. Exploration of this point is commonly referred to as the "forward problem." A majority of reports published on use of optical methods have focused on this issue for the purposes of detection, pattern recognition and patient monitoring (see [12] for a review). The directions these attempts have followed fall naturally into three general categories.

If the illumination strength at a fixed position and direction is constant in time, the quantities that may be measured are the position and direction dependence of the intensity of light at the surface. Measurement of the steady-state, or continuous wave (CW), distribution of light is relatively easy. The disadvantage is that the potential for spatial localization is reduced, as photons have the opportunity to propagate throughout the medium for any length of time prior to being detected.

A major goal of methods that fall into the second category is reduction of the variance of the distribution of paths of photon propagation through a medium to a detector. The common feature of these time-resolved techniques is that the detected light is studied as a function not only of position and (possibly) direction, but also of propagation time. Typically, these methods involve illumination with ultra-short pulses of light (fs-ps). The most valued component of the detected light is frequently, though not always, that which reaches the detector in the earliest time [13-15]. This is the fraction for which the variance of the propagation path distribution is smallest.

The third general category of methods have the common feature that the medium is illuminated with light whose intensity is a harmonic function in time. The intensity of the light detected at any point at the surface will also vary with the same frequency, but in general with a phase and ratio of AC amplitude to mean DC level different from the source [16,17]. It has been shown that these differences are functions of the optical cross-sections of the medium [18]. It is also possible, for simply structured media [19], to infer the mean of the propagation path distribution for light entering a detector from these measurements.

While our own work has extended to theoretical and experimental analyses of data from all three measurement types to varying extents, most, and all the data to be presented here, focuses on the first category. This emphasis follows from the premise that successful imaging of very deep structures or very thick media will unavoidably require making use of this type of information. This, in turn, is the conclusion drawn from studies of the rate of increase in propagation path variance with increasing propagation time [14], and of the decay of photon density waves with penetration distance [17].

2.1 Numerical Methods

The essential elements of the Monte Carlo model used in our simulations are sketched in Figure 1. Several well-known efficiency-enhancing techniques [20] are employed, including treating each simulated particle as an ensemble of photons; Russian roulette to terminate the histories of particles with low statistical weight; correlated sampling to distinguish the true effect of a change in the medium's properties from simple statistical variance; and extrapolating a photon's trajectory to the surface, and estimating the probability of it escaping, so that (on average) half of the simulated scattering events yield scoring events.

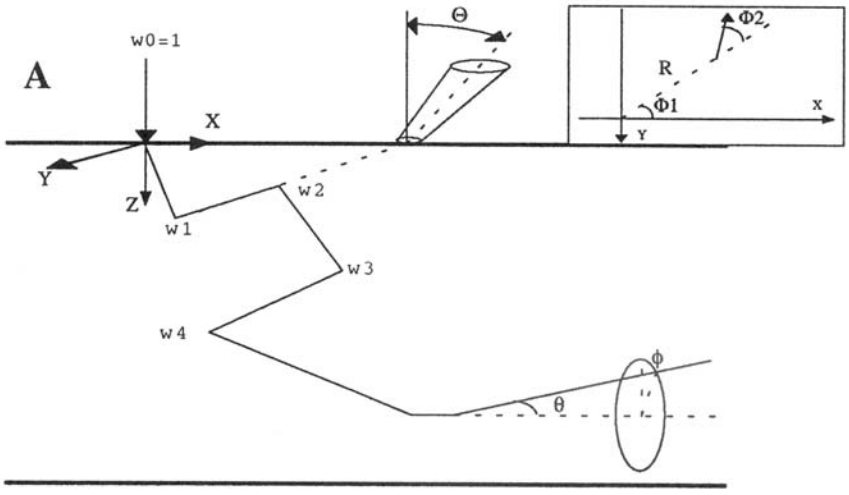

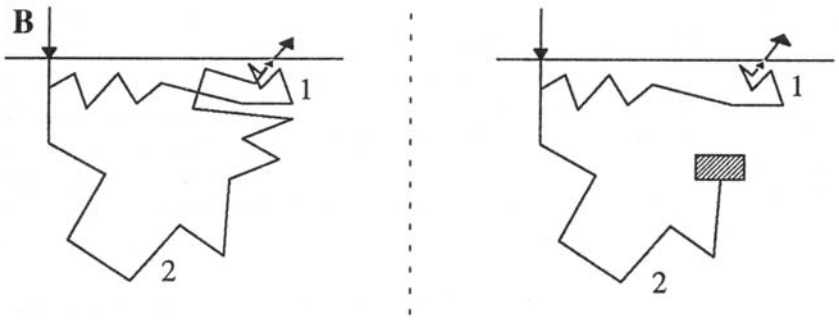

Legend to Figure 1 Monte Carlo model for simulating detector responses. Panel A: source and detector geometries, coordinate systems, and methods used to improve efficiency. All photons enter medium along positive z-axis; surface lies in the x-y plane. Detector counts photons exiting in a 1-mfp^2 (mfp = mean free path) area centered at point **R**, and whose exit directions lie in a specified solid angle. Inclination of central axis from normal is angle Θ. Inset: "bird's-eye" view of surface, showing distance of R from source to detector, and azimuthal angles Φ_1 and Φ_2 that complete the specification of the detector orientation. The distance a photon propagates between two successive collisions is given by: $d = m\ln\left[1/\left(1 - \left(1 - e^{-s_b/m}\right)X_1\right)\right]$, where m is the mfp, s_b is the distance from the starting position to the boundary along the current line of propagation, and X_1 is a random variable with uniform distribution between 0 and 1. The photon's weighting factor, initially 1, is reduced at each collision by $w_n = w_{n-1}(1 - p_a)(1 - e^{-s_b/m})$, where p_a is the absorption probability Σ_a/Σ_t. The change in direction due to scattering is determined by the formulas:

$$\theta = \cos^{-1}\left((2g)^{-1}\left[1 + g^2 - \left(\left[1 - g^2\right]/\left[1 + g(2X_2 - 1)\right]\right)^2\right]\right),$$

$$\phi = \pi(2X_3 - 1),$$

where g, the anisotropy factor, is the mean value of $\cos\theta$, and X_2 and X_3 are random variables identically distributed as X_1. These angles are converted to the angles of the fixed reference system by the formulas:

$$\Theta_n = \cos^{-1}(\cos\Theta_{n-1}\cos\theta - \sin\Theta_{n-1}\sin\theta\cos\phi),$$

$$(\Phi_1 + \Phi_2)_n = (\Phi_1 + \Phi_2)_{n-1} + \tan^{-1}\left[\sin\phi/(\cos\phi\cos\Theta_{n-1} + \cot\theta\sin\Theta_{n-1})\right],$$

where n is the number of collisions the photon has had in the medium, and $\Theta_0 = \pi$, $(\Phi_1 + \Phi_2)_0 = 0$. If the distance from the photon to the illuminated surface decreases along the post-scattering direction, its trajectory is extrapolated to the surface. The appropriate detector receives a score of $S = w_n\left(1 - e^{-s_d/m}\right)$, where s_d is the distance from the site of the n^{th} collision to the detector; this value is added to the sum of previous scores accumulated by the same detector. Panel B: correlated sampling for detecting the effect of a localized heterogeneity. Each simulated photon in the heterogeneous medium (right) follows exactly the same path as one in the corresponding homogeneous reference (left) unless it is absorbed. Photon 1 in this sketch contributes a score to the indicated detector in both media, while photon 2 scores only on the left and is absorbed on the right.

Simulation results have shown that selective probing of a turbid medium can be performed, even in the limiting case of isotropic scattering [21,22]. The optimal source-detector configuration (SDC) combines a pencil-beam source and a highly collimated detector receiving light from only a very small area on the surface of the specimen. Results shown in Figures 2 and 3 indicate the degree of selectivity achieved in this way. The most important determinant of the region preferentially probed by the detected light is the distance between the source and detector. This is a result that has also been demonstrated with analyses that approximated photon migration as a random walk on a three-dimensional lattice [23,24], and by diffusion theory [25]. The Monte Carlo simulations further reveal that finer selectivity can be obtained by also varying the orientation of the detector.

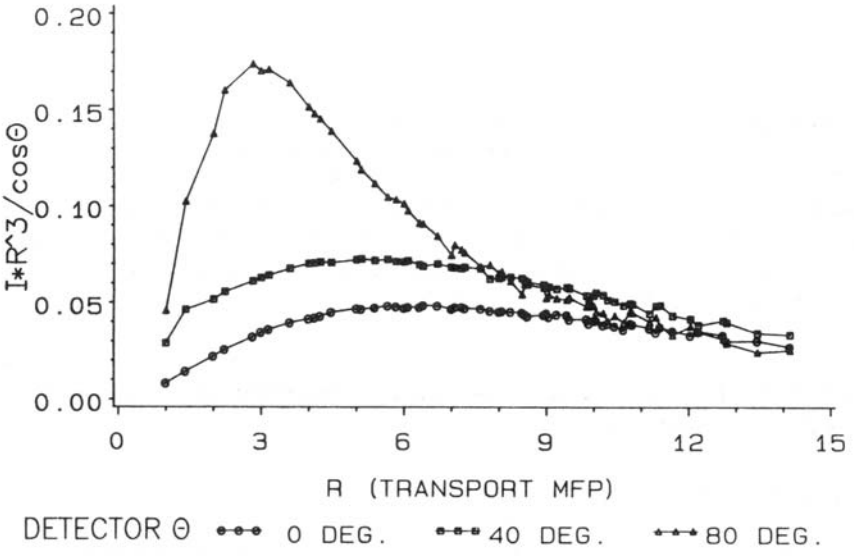

Legend to Figure 2 Effect of R and Θ on detected angular intensity. Curves show $R^3I/\cos\Theta$ *vs.* R for the indicated values of Θ. *I* is given in units of # photons detected/incident photon/mfp^2/sr; the 1/cosΘ factor compensates for reduction in detector aperture as its proceeds from normal to grazing inclination. Detectors counted photons whose exit directions deviated no more than 10° from the orientation of the central axis. The medium was homogeneous, with thickness 10 mfp and $\Sigma_a = .01\Sigma_t$. The plotted quantity appears to approach a constant value as R increases, as is predicted by diffusion theory. However, the behavior at small R is highly dependent on detector orientation.

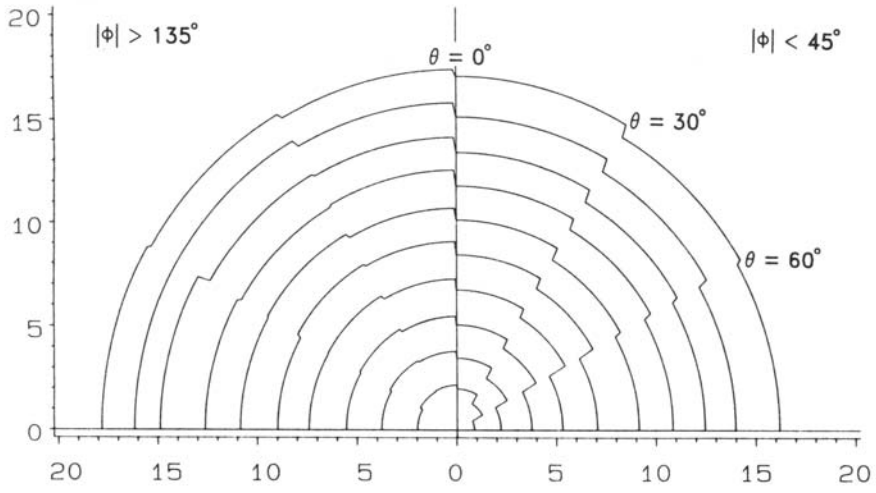

Legend to Figure 3 Effect of R and detector orientation on average maximum depth of detected photons. The greatest depth, Z, attained by each photon was recorded, and the average value $\langle Z \rangle$ for all photons counted by each detector was calculated after the simulation was completed. The acceptance solid angle of each detector was a spherical sector with $\Delta\Theta = 30°$ and $\Delta\Phi_2 = 90°$. The medium was homogeneous, with thickness 32 mfp and $\Sigma_a = 0$. Plotted curves are polar plots of $\langle Z \rangle$ *vs.* Θ. Each curve shows data for a different R; $\langle Z \rangle$ is the distance from the pole to the curve. (Reprinted from reference 5.)

3. IMPACT OF INTERNAL OPTICAL PROPERTIES ON ANGULAR INTENSITY AT SURFACE

3.1 Weight Functions – Theory

Consider a medium divided into a set of N small, contiguous, non-overlapping volume elements, or voxels. The voxel shapes are arbitrary, and they are sufficiently small that the optical properties do not vary significantly within a voxel. If a property affecting photon propagation is varied, the detected signal will also change; it is reasonable to expect the change in detected signal is a sufficiently smooth function of the voxels' properties that it may be expanded into a Taylor series:

$$y = y^0 + \sum_{i=1}^{N} \frac{\partial y^0}{\partial x_i}\left(x_i - x_i^0\right) + \frac{1}{2}\sum_{i=1}^{N}\sum_{j=1}^{N} \frac{\partial^2 y^0}{\partial x_i \partial x_j}\left(x_i - x_i^0\right)\left(x_j - x_j^0\right) + \ldots, \qquad (3)$$

where y is the detected signal, x is the property being varied within the medium (absorption cross-section, scattering cross-section, scattering anisotropy, total cross-section, refractive index, *etc.*), the summations are performed over all voxels in the medium, and the superscript 0 indicates the values that exist in the initial, or reference, state. An expansion of the type in eq. 3 is also known as a perturbation series. The

second term on the right-hand side describes the primary, or first-order, effect of altering the property x. The third term describes second-order effects, with each second partial derivative in the summation giving the strength of the interaction between a pair of voxels (or the effect of a voxel on itself in the case of $i=j$). That is, the effect that altering x in voxel i has on the light intensity at points within and in the immediate vicinity of voxel j. Higher-order terms, likewise, describe interactions among larger numbers of voxels.

It is useful to introduce a linearity assumption. The physical statement of this assumption is that the combined effect of any number of voxels on a detected signal is just the algebraic sum of the effects of the voxels taken individually. The mathematical statement is that only the first-order derivatives in eq. 1 are non-zero. This will be approximately valid if all the $\left(x_i - x_i^0\right)$ are small, in which case it is appropriate to truncate eq. 3 after the linear term, and rearrange it to obtain:

$$y^0 - y = \sum_{i=1}^{N}\left(-\frac{\partial y^0}{\partial x_i}\right)\left(x_i - x_i^0\right), \text{ or}$$

$$\Delta y = \mathbf{w}^T \Delta \mathbf{x} \qquad (4)$$

The vector $\mathbf{w}$ is referred to as a "weight function" for the optical property under consideration. In other areas of physics, quantities analogous to $\mathbf{w}$ have been called "contributons" or "importance functions" [26,27]. In our applications, the detected quantity y is the intensity of the light exiting the surface of the medium. The optical property x that has been the primary focus of our attention so far is Σ_a, the macroscopic absorption cross-section.

3.2 Derivation and Calculation of Weight Functions

3.2.1 Weight Function for the CW Case

If the Σ_a of a voxel is varied over a large range, and yet has no significant impact on the intensity of detected light, there are two possible (not mutually exclusive) explanations. One is that no appreciable fraction of the photons entering the medium from the source propagate into the voxel containing the variable absorption. The second is that no appreciable fraction of the photons that emerge from that voxel exit the medium within the field of view of the detector. This indicates that the weight is proportional to the product of two independent functions, one being the intensity of light within a voxel due to a light source of unit strength at the surface, and the other being the intensity of light at the detector due to a source of unit strength placed inside the voxel. Let:

$\psi(\vec{r})$ = collision density at point $\vec{r}$ in the medium (collisions / unit volume / photon).

$P_j(\vec{r})$ = contribution to the angular intensity in detector j due to one photon emitted isotropically at $\vec{r}$ per second (photons / unit area / unit solid angle).

$\Sigma_t(\vec{r})$ = macroscopic total cross-section at $\vec{r}$ (distance^{-1}).

$\Delta\Sigma_a(\vec{r})$ = macroscopic absorption cross-section difference at $\vec{r}$, between sample and reference media (distance^{-1}).

ΔI_j = decrease in intensity at detector j due to absorption.

If the assumption of linearity is valid, then $\psi(\vec{r})$ and $P_j(\vec{r})$ are computed for the reference medium, and ΔI_j is equal to :

$$\Delta I_j = \int \frac{\Delta\Sigma_a(\vec{r})}{\Sigma_t(\vec{r})} \psi(\vec{r}) P_j(\vec{r}) dV \ , \tag{5}$$

or, since the medium is taken to consist of discrete voxels with constant optical properties within each voxel:

$$\Delta I_j = \sum_i \frac{\Delta\Sigma_{ai}}{\Sigma_{ti}} \psi_i P_{ij} V_i \ . \tag{6}$$

As written, eq. 5 and eq. 6 are strictly correct only for the case of isotropic scattering. For almost all of the image reconstructions subsequently carried out, this was the assumption made about the scattering property of the medium. These equations are readily generalized to cases of anisotropic scattering: ψ and P_j are functions of Ω as well as of $\vec{r}$, and the products of the two in eq. 5 (6) must be replaced by an double integral (summation) over all directions, with the integrand being the product of $\psi(\vec{r},\hat{\Omega})$, $P_j(\vec{r},\hat{\Omega}')$, and $f(\hat{\Omega},\hat{\Omega}')$, the differential cross-section for scattering from direction Ω into direction Ω'.

The quantity $\psi_i V_i$, which is simply the absorption rate in voxel i, can readily be computed by Monte Carlo. The calculation of P_{ij} is made tractable by employing a reciprocity theorem that says:

$$G(\vec{R}_j,\hat{\Omega}_j;\vec{r},\hat{\Omega}) = G(\vec{r},-\hat{\Omega};\vec{R}_j,-\hat{\Omega}_j) \ ,$$

where $\vec{R}_j$ is the location of detector j on the surface, $\hat{\Omega}_j$ is the direction of the light it detects, and $G(\vec{r}_1,\hat{\Omega}_1;\vec{r}_2,\hat{\Omega}_2)$ is the angular intensity at $\vec{r}_1$ in direction $\hat{\Omega}_1$, per unit solid angle, due to one photon emitted at $\vec{r}_2$ in direction $\hat{\Omega}_2$. From this it follows that the contribution of each collision in voxel i to P_{ij} is just $1/4\pi$ times the total intensity at $\vec{r}$

due to a single photon launched into the medium from detector j, *i.e.*, in the reverse direction from $\hat{\Omega}_j$.

To rewrite eq. 4 in terms of quantities calculated by Monte Carlo simulations, let:

F_{0i} = number of collisions in V_i due to a single photon launched from the source.
F_{ij} = number of collisions in V_i due to a single photon launched from the detector.
S_{0j} = source strength (photons / second).

Then:

$$S_{0j}F_{0i} = \psi_i V_i$$
$$F_{ij} = 4\pi P_{ij}\Sigma_{ti}V_i .$$

So the change in intensity at the detector is:

$$\Delta I_j = \frac{S_{0j}}{4\pi}\sum_i \frac{\Delta\Sigma_{ai}}{\Sigma_{ti}^2 V_i}F_{0i}F_{ij} ,$$

If the unknown quantity to be found in voxel i is Σ_{ai}, the weight is:

$$w_{ij}^{cw} = \frac{S_{0j}F_{0i}F_{ij}}{4\pi\Sigma_{ti}^2 V_i} , \qquad (7)$$

which is acceptable if Σ_t is known for each voxel. In the general case, the expression for the weight would also contain terms describing the effect on detected intensity of a small change in the scattering cross-section and in the cross-sections for any other processes that occur to a significant extent. Eq. 7 is also the weight relating the intensity of fluorescent light measured at detector j due to a fluorescent source of unit strength in voxel i.

3.2.2 Absorption and Fluorescence Weight Functions, Time-Resolved Case

When a medium is illuminated by a brief pulse of light, the intensity in voxel i is a function of time following the pulse. Likewise, the contribution to the signal detected at detector j from light emitted by voxel i at a given instant is a function of time. The weight function corresponding to a given source, detector, and voxel then is a function of time as well. The generalization of eq. 7 to the time-resolved case can not be proportional to a simple product of two collision densities as in the CW case. If t denotes the total time that passes between a photon entering a medium and its subsequent detection, the weight function calculation must take account of all possible pairs of source-to-voxel time and voxel-to-detector time that sum to t. If τ is the time that passes

between the photon entering the medium and having a collision in voxel i, the absorption weight function for the time-resolved case is:

$$w_{ij}(t) = \frac{S_{0j}}{4\pi\Sigma_{ij}^2 V_i}\int_0^t F_{0i}(\tau)F_{ij}(t-\tau)d\tau\,. \tag{8}$$

The product in eq. 7 has been replaced here by a convolution integral. F_{0i} is zero for values of τ below a certain critical value, and F_{ij} is zero when τ is larger than a second critical value. It should be noted this means the lower and upper integration limits in eq. 8 may be replaced by $-\infty$ and ∞, respectively, without changing the result.

The corresponding weight function can also be derived for measurements of time-resolved fluorescence. There is an additional complication in the calculation of the appropriate weight function, as the lifetime of the excited state of a fluorophore is also variable. Typically, the probability density function for a fluorophore to emit a time t after absorbing a photon is of the form $e^{-t/\tau_0}/\tau_0$, where the mean lifetime τ_0 is typically on the order of 10 ns. Then the weight function must take account of all possible sets of source-to-absorption, absorption-to-emission, and emission-to-detector times that sum to t. The extension of eq. 8 to this case is:

$$w_{ij}(t) = \frac{S_{0j}}{4\pi\Sigma_{ij}^2 V_i \tau_0}\int_0^t F_{0i}(\tau)\int_0^{t-\tau} e^{-\tau'/\tau_0}F_{ij}(t-\tau-\tau')d\tau' d\tau\,. \tag{9}$$

3.2.3 Weight Function for the frequency-domain (fd) case

If a medium is illuminated by a source whose intensity varies sinusoidally about its mean value (*i.e.*, an AM signal), the change in the DC component, AC amplitude, and AC phase at detector j caused by changing Σ_a in voxel i can be calculated from the CW and time-resolved weight functions. If the phase of the source is taken to be 0, then:

$$\begin{aligned} w_{ij}^{fd} &= w_{ij}^{cw} + w_{ij}(\omega,t) \\ &= w_{ij}^{cw} + \frac{\sqrt{2\pi}}{v}\left(f_R(\omega)\cos\omega t - f_I(\omega)\sin\omega t\right), \end{aligned} \tag{10}$$

where v is the speed of light in the medium, and $f_R(\omega)$ and $f_I(\omega)$ are, respectively, the real and imaginary parts of the Fourier transform of the time-resolved weight function. Because the limits of integration in eq. 7 and eq. 8 (outer integral in the latter case) can be changed to $-\infty$ and ∞, the convolution rule for Fourier transforms may be used in the calculation of $f_R(\omega)$ and $f_I(\omega)$.

3.3 Examples of Weight Function Calculations

The model used for the Monte Carlo calculations of collision density is sketched in Figure 4. The scoring was simpler here than for the calculation of detector responses sketched in Fig. 1, as here each voxel was a "detector" and kept a count of how many collisions took place within its boundaries, irrespective of the directions of motion of the photons (see Fig. 4A). When cylindrical media were modeled, each voxel, as shown in Fig. 4B, was a sector of a circular annulus, proceeding in shape from a circular disk at the center through shapes that approach rectangular parallelepipeds in the limit as the distance from the cylinder axis increases without bound. Each of these voxels has a volume of $\pi/4$ mfp^3.

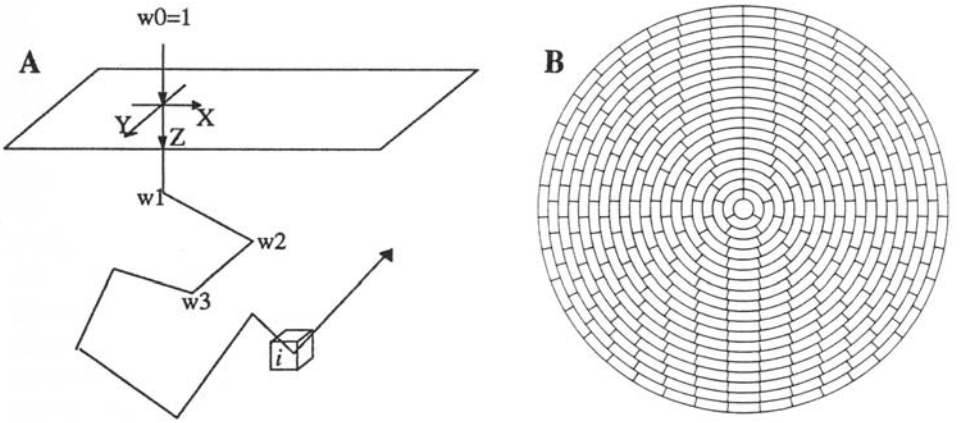

Legend to Figure 4 Panel A: Monte Carlo model for calculating collision density distributions. As in detector response simulations (see Fig. 1), photons are forced to remain within the boundaries of the medium; the weighting factor w_n, initially 1.0, is reduced on each collision to account for the probabilities of absorption and of loss through the boundary. When the n^{th} collision occurs in voxel i, the voxel's score (initially 0) is increased by w_n. Collision density units are # collisions/incident photon/mfp^3. Panel B: voxel grid used collision density calculation in cylindrical medium. Shown is a 2-D slice $\perp$ cylinder axis; cylinder radius in this illustration is 10 mfp. Volume of each voxel is $\pi/4$ mfp^3.

Examples of weight functions calculated for slab-type media have been described previously [6,7]. Examples of weight functions calculated for cylindrical media are shown in Figure 5. All are for the CW case, and for sources and detectors directed normally to the surface. The cases shown illustrate the effects of varying the cylinder radius, the angle between the source and detector axes, and the refractive-index mismatch between the cylinder and its surroundings. Also studied (data not shown) was the effect of varying the anisotropy of the scattering.

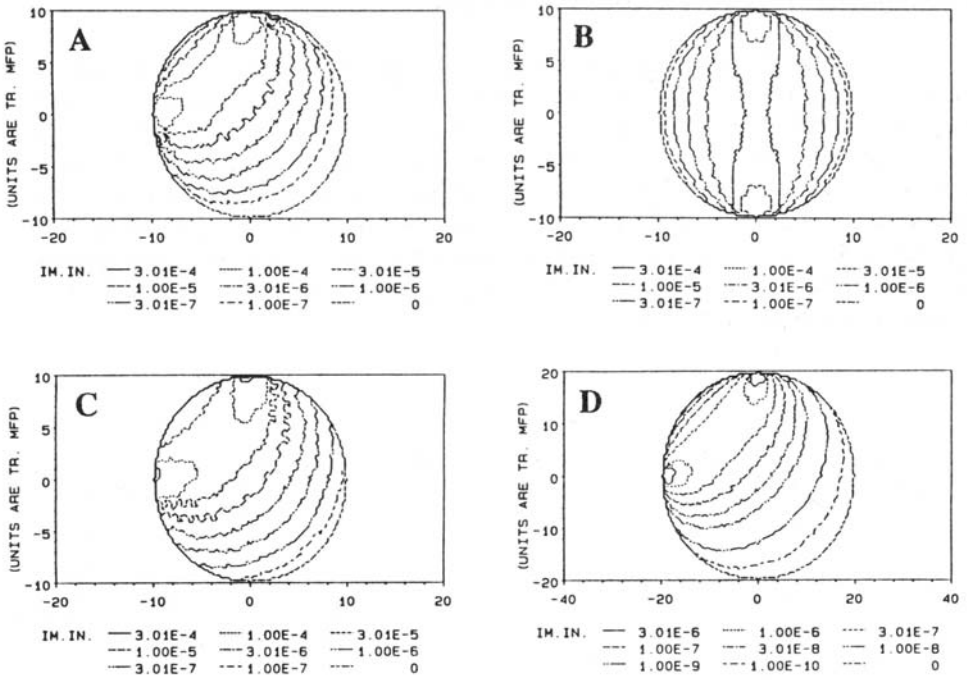

Legend to Figure 5 2-D sections through CW cylinder weight functions. In all examples shown here, source and detector axes lay in the plane of section, ⊥ cylinder axis, and normal to the surface. Panel A: cylinder radius is 10 equivalent isotropic step lengths, angle α between source and detector axes is 90°, refractive index is 1.0 inside and outside the cylinder. Panel B: cylinder radius is 10 equivalent isotropic step lengths, angle α between source and detector axes is 180°, refractive index is 1.0 inside and outside the cylinder . Panel C: cylinder radius is 10 equivalent isotropic step lengths, angle α between source and detector axes is 90°, refractive index is 1.33 inside the cylinder, 1.0 outside. Panel D: cylinder radius is 20 equivalent isotropic step lengths, angle α between source and detector axes is 90°, refractive index is 1.0 inside and outside the cylinder.

4. IMAGE RECONSTRUCTION

4.1 Reconstruction as Solution of a Linear System

For the purpose of reconstructing images of absorption cross-section based on intensity readings, eq. 4 becomes:

$$\Delta I_j = \mathbf{w}_j^T \Delta\Sigma_a ,$$

where the subscript j is an index defining the particular SDC under consideration, and $\mathbf{w}$ is the weight function given by eq. 7 for a CW measurement of ΔI or by (a discretized version of) eq. 6 for a time-resolved measurement of ΔI. If the number of independent

measurements is equal to the number of voxels in the medium, then they combine to give a fully-determined system of linear equations:

$$\Delta \mathbf{I} = \mathbf{W}\Delta\Sigma_a \tag{11}$$

This validity of this linear system depends upon that of the assumption that the properties of the medium under study are a sufficiently small perturbation of those of the reference state. The meaning of "sufficiently small" is not yet well-established, however, and the usefulness of eq. 11 is not as limited as it may at first appear (see Discussion).

The dependence of the detected intensity on a change in the Σ_a of a given voxel for any of the measurement types considered here, and the formulas for the corresponding weight functions, are summarized in Table 1.

4.2 Solution of Perturbation Equation

In an accompanying paper [28], various approaches to solving equation 11 are presented. Other efforts at imaging using perturbation approaches are described in [29,30]. Here we describe results based on evaluation of detector readings that were normalized ($1 - I/I_0$), instead of their absolute differences (ΔI). This substitution, while yielding a different, although correlated, result, avoids the difficulties associated with fluctuations in source strength and imperfect detector calibration. Essentially, we apply an extension of the back-projection algorithm used in CT, where the matrix of spatial weighting functions is substituted for line integrals. In each voxel the products of the measured relative attenuation and the weight are calculated for all SDC's. After this is done for all SDC's, the value assigned to a given voxel i is:

$$\sum_j w_{ij}\left(1-I/I_0\right)_j ,$$

where j is the SDC index. This result needs to be modified to account for the gradient in weight that is always present, w decreasing with increasing depth. The image intensity is calculated by dividing the previous result by the sum, over all SDC's, of the weight in voxel i, to give:

$$\sum_j w_{ij}\left(1-I/I_0\right)_j \Big/ \sum_j w_{ij} .$$

This operation is known to yield a convolved image. An iterative correction procedure was employed to yield an improved result. The mathematical formulation of the algorithm is:

Measurement type	Weight	Perturbation Equation
steady– state	$w_{ij}^{cw} = \frac{S_{0j} F_{oi} F_{ij}}{4\pi \Sigma_n^2 V_i}$	$\Delta I_{ij} = w_{ij}^{cw} \Delta \Sigma_{ai}$
time domain, absorption	$w_{ij}(t_1 - t_2) = \frac{S_{0j}}{4\pi \Sigma_n^2 V_i} \int_{t_1}^{t_2} \int_0^t F_{0i}(\tau) F_{ij}(t-\tau) d\tau dt$	$\Delta I_{ij}(t) = w_{ij}(t) \Delta \Sigma_{ai}$
time domain, fluorescence	$w_{ij}(t_1 - t_2) = \frac{S_{0j}}{4\pi \Sigma_n^2 V_i \tau_0} \int_{t_1}^{t_2} \int_0^t F_{0i}(\tau) \int_0^{t-\tau} e^{-\tau'/\tau_0} F_{ij}(t-\tau'-\tau) d\tau' d\tau dt$	$I_{ij}(t) = w_{ij}(t) F_i$
frequency domain	$w_{ij}(\omega, t) = \frac{\sqrt{2\pi}}{v} \left[\Re\left(FT\left[w_{ij}(t) \right] \right) \cos \omega t - \Im\left(FT\left[w_{ij}(t) \right] \right) \sin \omega t \right]$	$\Delta I_{ij}(\omega, t) = \left[w_{ij}^{cw} + w_{ij}(\omega, t) \right] \Delta \Sigma_{ai}$ $I_{ij}(\omega, t) = \left[w_{ij}^{cw} + w_{ij}(\omega, t) \right] F_i$

Legend to Table 1 Weight function formulas and perturbation equations for CW, time-resolved, and frequency-domain measurements of either absorption or fluorescence. Expressions in second column show how weight functions are to be calculated from quantities readily measured experimentally or determined from simulations. For CW measurement, weight function formula is the same for both absorption and fluorescence measurements. Expressions in third column show the first-order effect of a change in absorption, or of a fluorescent source, in voxel i upon the intensity of light measured by detector j.

$$s_i^n = s_i^{n-1} + \frac{\sum_j w_{ij}\left[\left(\frac{\Delta I}{I_0}\right)_j - c_j^{n-1}\right]}{\sum_j w_{ij}} \tag{12a}$$

$$c_j^n = \frac{\sum_i w_{ij} s_i^n}{\sum_i w_{ij}} \tag{12b}$$

with $n \geq 1$, and $s_i^0 = 0$ for all voxels, $c_j^0 = 0$ for all SDC s. s_i^n is the estimate at iteration n of the image intensity in voxel i, c_j^n is the estimate at iteration n of the relative attenuation at SDC j, and I_{0j} is the intensity reading at SDC j for the reference medium. In practice, we usually impose a positivity constraint on s_i^n, for in the examples to be presented it was known *a priori* that the absorption of the test medium was at no point less than that of the reference medium. Convergence was assumed when the squared differences between estimates of c in successive iterations, summed over all j, fell below a preset threshold.

4.3 Numerical Validation

In an accompanying paper [28] and other recent reports [7-9], the accuracy and stability of the perturbation model has been examined using various test media by considering only the backscattered field. These studies have shown the model is relatively robust to a depth of at least 10 transport mean free paths (mfp) for small targets, even under conditions where the problem is highly underdetermined and seriously violates the assumption of a weak perturbation. In the following section we describe results of preliminary experimental studies that demonstrate the ability to image buried objects across the equivalent thickness of an uncompressed breast.

4.4 Experimental Validation

Experimental measurements were performed on a cylindrical phantom (see Fig. 4B) designed to approximate the degree of scattering and attenuation that would be present in an uncompressed breast. The cylinder wall is translucent plastic, ~8.6 cm o. d. and ~7.9 cm i. d., and it was filled to a height of ~35 cm with a suspension of Intralipid® that was either 2%, 0.4%, or 0.08% lipid by volume. The absorber was a hollow glass rod, 7 mm o. d. and 5 mm i. d., containing diluted india ink (1 mL ink to 7.5 mL H_2O), and held with its axis parallel to that of the cylinder, either at the center of the cylinder or at one of six positions ~2.25 cm from the center. Optical measurements were accomplished using a custom built multi-wavelength optical CT scanner. A Coherent 599 dye laser (1.5 mm beam dia.) was operated between 25-150 mW at 720 nm. Photon emission about the target was measured at 10° intervals by translating,

under computer control, a Hamamatsu 3140C CCD camera in a 190° arc starting from 40° from backscatter to 50° beyond full transmission, (see Figure 6, and 4B).

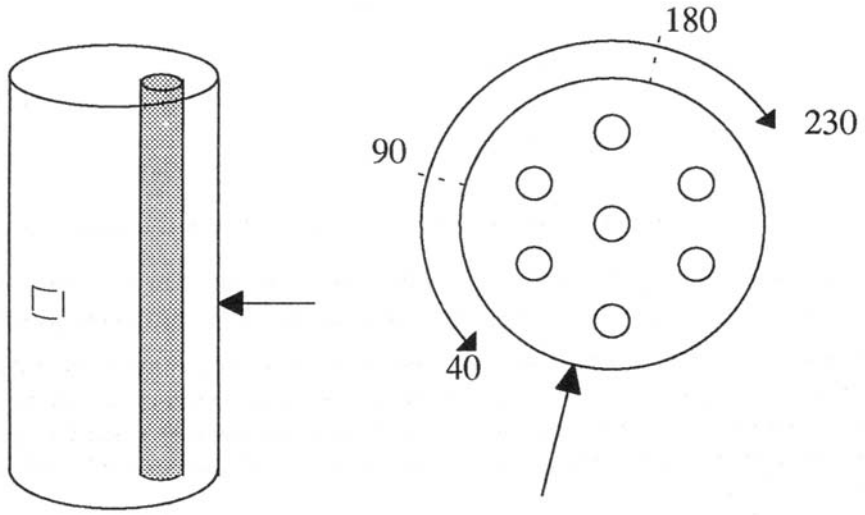

Legend to Figure 6 Sketch of phantom used to model thickness and optical properties of an uncompressed mammary. Left: lateral view (not to scale) of cylinder containing absorbing rod in an off-center site. Source (arrow) is a narrow beam of laser light normally incident on cylinder at about the midheight of the liquid column. CCD camera received light from a ~3.8 cm by ~3.2 cm area on the surface (see text for details on laser and camera). Only data from a 6 mm-high strip at the center of the field of view were used in image reconstruction. Right: end view (not to scale) of cylinder, showing seven possible locations of absorbing rod relative to cylinder axis and source beam (arrow), and arc through which camera revolved, 10° steps, as data were collected.

Independent measurements of the transport mfp and absorption length of the suspensions indicate the diameter of the cylinder was between 150 and 200 transport mfp when the concentration was 2% [31]. As this most closely matches the dimensions that are encountered using red or NIR light for imaging of breast, most of the examples of reconstructed images shown in Figure 9 and Figure 10 were produced from the measurements of the phantom containing this concentration of Intralipid®. The weight functions used were derived from Monte Carlo simulations of cylindrical media with absorption cross-section $\Sigma_a = .01\Sigma_t$. To test the sensitivity of the reconstruction algorithm to errors in the estimate of the optical properties of the reference media, reconstructions were carried out for four different assumed values of the diameter of the cylinder: 10, 20, 40, and 100 transport mfp. In some cases, reconstructions also were made with weight functions calculated for several different assumed values of the refractive index mismatch, in the range (1–1.5):1, between the cylinder and its surroundings.

The reconstructions shown in Figure 7 illustrate that highly accurate results are obtained for all cases examined when the rod is in the center of the cylinder. In each example shown, the weight function calculation was made with an assumption of

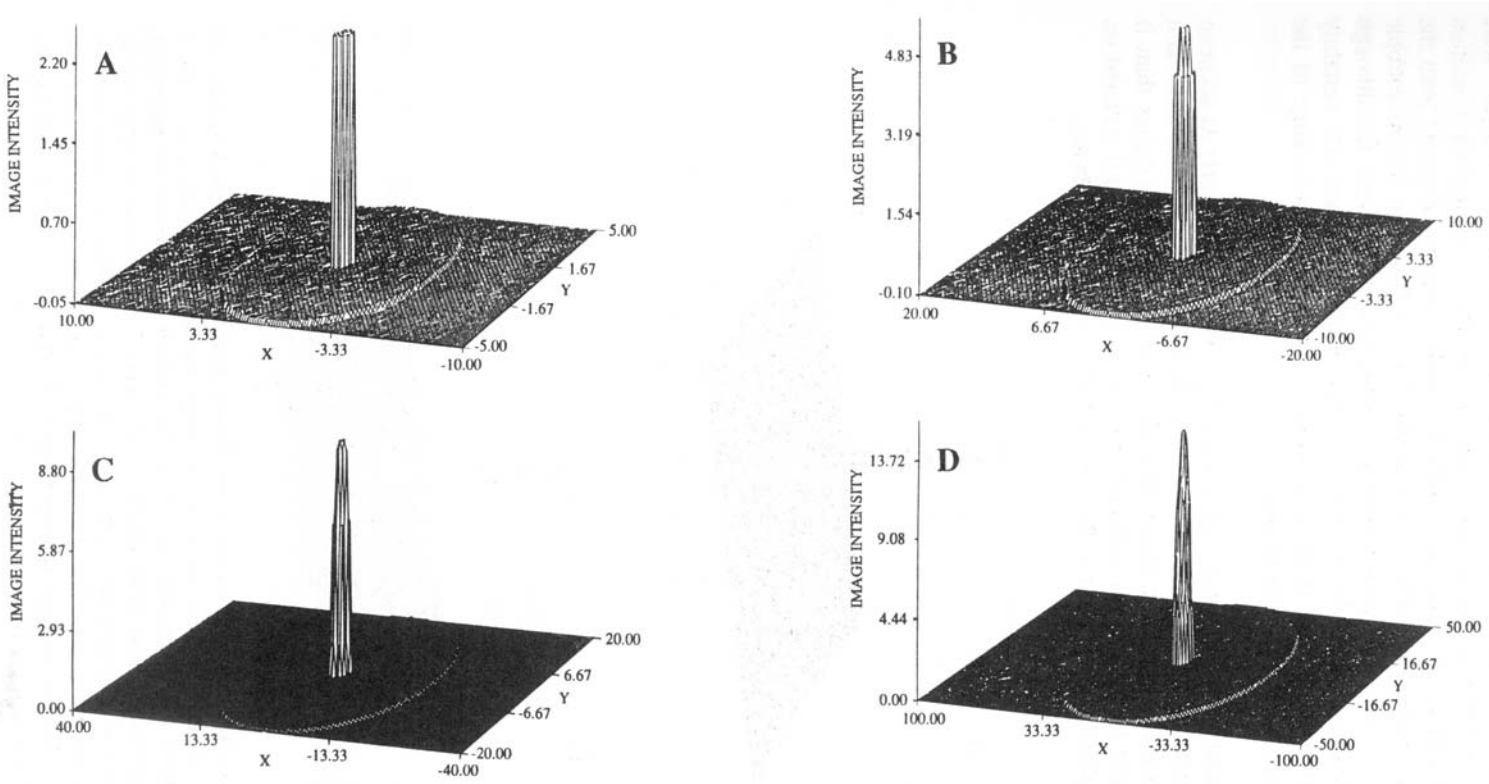

Legend to Figure 7 Image reconstructions for case of 2% Intralipid® concentration, absorbing rod at center of cylinder. Surfaces are plots of image intensity *vs.* distance in x and y directions; cylinder axis is at (0,0). In each case 10^4 iterations of a non-progressive reconstruction, using eq.'s 12, were performed. A positivity constraint was applied to the image intensity values. Assumptions made in weight function calculation were isotropic scattering, no internal reflection at boundary, $\Sigma_a = .01\Sigma_t$. Panel A: assumed cylinder radius is 5 equivalent isotropic step lengths. Panel B: assumed cylinder radius is 10 equivalent isotropic step lengths. Panel C: assumed cylinder radius is 20 equivalent isotropic step lengths. Panel D: assumed cylinder radius is 50 equivalent isotropic step lengths.

isotropic scattering. The only condition in which the reconstructed "images" were grossly inaccurate (not shown) was the use of weight functions calculated for a medium with highly forward-directed scattering, in which case the gradient of weight from the surface to the center of the cylinder was qualitatively different from that for the isotropic scattering case. Note that this does not invalidate the results shown here, for although individual scattering events in the suspension (and in breast tissue) are certainly anisotropic, the voxel dimensions in these reconstructions are at least as large as the equivalent-isotropic-step-size in these media.

The reconstructions shown in Figure 8 illustrate that results nearly as accurate as those for the centered-rod case are obtained for the off-centered rod case. There is a tendency for the region of greatest image intensity to be closer to the center than it would be in a perfect reconstruction, although it is of the correct size and centered on the radius at the correct angle relative to the direction of the illuminating beam.

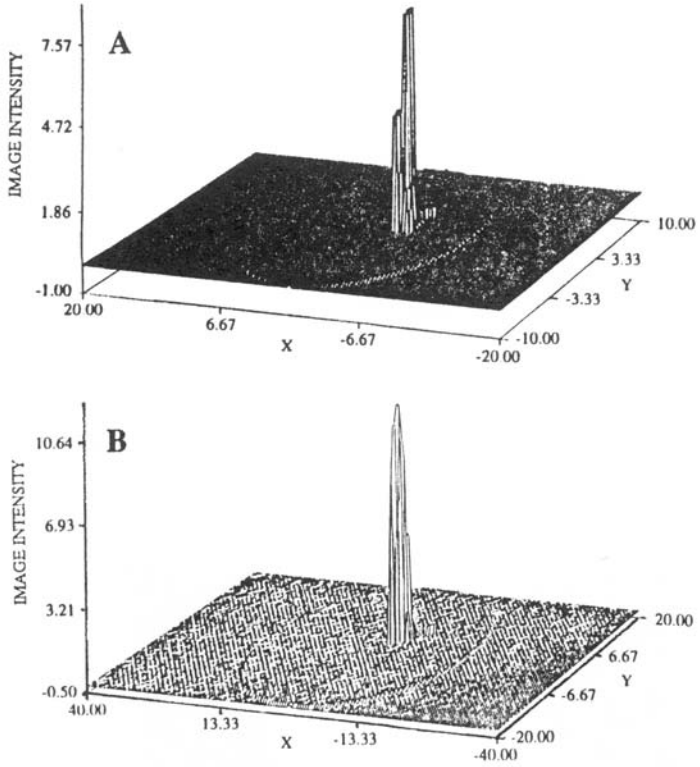

Legend to Figure 8 Image reconstructions for case of 2% Intralipid® concentration, absorbing rod at off-center site in cylinder. Surfaces are plots of image intensity *vs.* distance in x and y directions; cylinder axis is at (0,0). In each case 10^4 iterations of a non-progressive reconstruction, using eq.'s 12, were performed. A positivity constraint was applied to the image intensity values. Correct location and size of absorbing rod are indicated by a region of negative image intensity. Assumptions made in weight function calculation were isotropic scattering, no internal reflection at boundary, $\Sigma_a = .01\Sigma_t$. Panel A: assumed cylinder radius is 10 equivalent isotropic step lengths. Panel B: assumed cylinder radius is 20 equivalent isotropic step lengths.

The images in Figure 9 are an explicit demonstration of improvement in image quality upon using a progressive (Fig. 9B) rather than a non-progressive (Fig. 9A) reconstruction. In the former case, only data from SDC's with the smallest value of the angle α between the source and detector axes (40°) were used in the reconstruction at first. Data from SDC's with successively larger α (10° steps) were added sequentially, after a preset number of iterations each time. In this example, no attempt was made to fix the values of image intensity in voxels near the surface following early stages of the reconstruction.

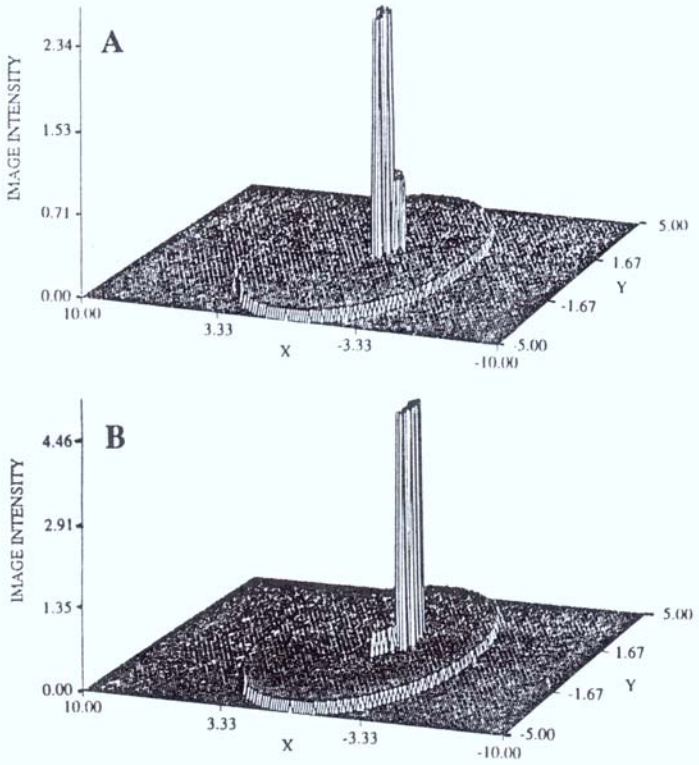

Legend to Figure 9 Improved image reconstruction, case of 2% Intralipid® due to use of progressive algorithm. Surfaces are plots of image intensity *vs.* distance in x and y directions; cylinder axis is at (0,0). A positivity constraint was applied to the image intensity values. Assumptions made in weight function calculation were isotropic scattering, no internal reflection at boundary, $\Sigma_a = .01\Sigma_t$. Assumed cylinder radius is 5 equivalent isotropic step lengths. Panel A: image after 10^4 iterations of non-progressive reconstruction. Panel B: image after 10^4 iterations of progressive reconstruction.

5. DISCUSSION AND FUTURE DIRECTIONS

The images shown here were reconstructed from measurements of media with high absorption contrast between the heterogeneity and the background. We chose this,

in part, to assess the effects that large violations in the linearity assumption have on the resultant image. The errors seen in the reconstructed images are, however, quantitative not qualitative in nature. The only case in which clearly unsatisfactory results were obtained occurred when the weight functions used had a qualitatively incorrect gradient, with the weight larger in voxels near the center than in those near the surface. This observation would suggest that estimates of weight functions having the correct direction of gradient may be sufficient for locating objects buried deeply in a highly scattering medium, at least for simply structured media.

As described above, we have derived here expressions for weighting functions capable of evaluating data from amplitude modulated measurements and fluorescence measurements performed in either the steady-state, time domain, or frequency domain. In comparison to evaluation of absorption-scattering data, the fluorescence problem has several features that appear especially attractive for an imaging scheme. First, the ability to filter out scattered incident photons suggest that the sensitivity to a given point, especially deep in the medium, could be greatly improved. Second, because emission is induced by an external source, the strength of this signal will depend strongly on the position of the fluorophore in relation to the source. Thus, unlike the nuclear medicine problem, an additional degree of freedom exists from which to derive spatial information. Third, in the time domain, it seems plausible to look for differences, along the surface, in the time of arrival of fluorescence in response to a train of ultra-fast pulses. Fourth, by linking appropriate fluorescent probes to antibodies or other biomolecules, significant enhancement of specificity is plausible.

Finally, while we have emphasized here and elsewhere [7-9] the merits of inversion schemes derived from particle transport models, recent reports by O'Leary *et al.* [32], demonstrating refractive behavior of photon density waves, may indicate that direct evaluation of wave phenomena is possible. Rigorous analysis would be obtained by using the Helmholtz equation. Recent reports by Klibanov *et al.* [33,34] demonstrating that, under favorable circumstances, good quality images can be obtained using a computationally efficient iterative scheme derived from the Helmholtz equation are promising.

6. REFERENCES

1. A. Ishimaru, *Wave Propagation and Scattering in random Media*, Academic Press, Orlando, 1978.

2. K. M. Case, P. F. Zweifel, *Linear Transport Theory*, Addison-Wesley, 1967.

3. R. L. Barbour, J. Lubowsky, H. Graber, "Use of reflectance spectrophotometry as a possible 3-dimensional spectroscopic imaging technique," FASEB J., vol. 2, p. a1772, 1988.

4. R. L. Barbour, J. Lubowsky, R. Aronson, "Method of imaging a random medium," U.S. Patent no. 5,137,355 (filed June 8, 1988; issued Aug. 11, 1992).

5. R. L. Barbour, H. Graber, R. Aronson, J. Lubowsky, "Model for 3-D optical imaging of tissue," proc. 10th Annual International Geoscience and Remote Sensing Symposium (IGARSS), vol. II, pp. 1395-1399, 1990.

6. R. L. Barbour, H. L. Graber, R. Aronson, J. Lubowsky, "Imaging of subsurface regions of random media by remote sensing," *Time-Resolved Spectroscopy and Imaging of Tissues*, SPIE vol. 1431, pp. 192-203, 1991.

7. R. L. Barbour, H. L. Graber, J. Lubowsky, R. Aronson, B. B. Das, K. M. Yoo, R. R. Alfano, "Imaging of diffusing media by a progressive iterative backprojection method using time-domain data," *Physiological Monitoring and Early Detection Diagnostic Methods*, SPIE vol. 1641, pp. 21-34, 1992.

8. Y. Wang, J. Chang, R. Aronson, R. L. Barbour, H. L. Graber, J. Lubowsky, "Imaging of scattering media by diffusion tomography: an iterative perturbation approach," *Physiological Monitoring and Early Detection Diagnostic Methods*, SPIE vol. 1641, pp. 58-71, 1992.

9. J. Chang, Y. Wang, R. Aronson, H. L. Graber, R. L. Barbour, "A layer-stripping approach for recovery of scattering media from time-resolved data," *Inverse Problems in Scattering and Imaging*, SPIE vol. 1767, pp. 384-395, 1992.

10. B. D. Steinberg, *Microwave Imaging with Large Antenna Arrays*, John Wiley & Sons, New York, 1983.

11. A. Schatzberg, A. J. Devaney, "Super-resolution in diffraction tomography," Inverse Problems, vol. 8, pp. 149-164, 1992.

12. B. Chance, "Optical Method," *Annual Reviews of Biophysics and Biophysical Chemistry 20*, pp. 1-28, 1991.

13. J. C. Hebden, R. A. Kruger, "Transillumination imaging performance: a time-of-flight imaging system," Medical Physics, vol. 17, pp. 351-356, 1990.

14. P. P. Ho, P. Baldeck, K. S. Wong, K. M. Yoo, D. Lee, R. R. Alfano, "Time dynamics of photon migration in semiopaque random media," Applied Optics, vol. 28, pp. 2304-2310, 1989.

15. B. Chance, J. S. Leigh, H. Miyake, D. S. Smith, S. Nioka, R. Greenfeld, M. Finander, K. Kaufmann, W. Levy, M. Young, P. Cohen, H. Yoshioka, R. Boretsky, "Comparison of time-resolved and -unresolved measurements of deoxyhemoglobin in brain," PNAS, vol. 85, pp. 4971-4975, 1988.

16. J. Fishkin, E. Gratton, M. J. vandeVen, W. W. Mantulin, "Diffusion of intensity modulated near-infrared light in turbid media," *Time-Resolved Spectroscopy and Imaging of Tissues*, SPIE vol. 1431, pp. 122-135, 1991.

17. L. O. Svaasand, B. Tromberg, "On the properties of optical waves in turbid media," *Future Trends in Biomedical Applications of Lasers*, SPIE vol. 1525, pp. 41-51, 1991.

18. K. W. Berndt, J. R. Lakowicz, "Detection and localization of absorbers in scattering media using frequency-domain principles," *Time-Resolved Spectroscopy and Imaging of Tissues*, SPIE vol. 1431, pp. 149-160, 1991.

19. E. M. Sevick, B. Chance, J. Leigh, S. Nioka, M. Maris, "Quantitation of time- and frequency-resolved optical spectra for the determination of tissue oxygenation," Anal. Biochem., vol. 195, pp. 330-351, 1991.

20. M. H. Kalos, P. A. Whitlock, *Monte Carlo Methods, vol. 1: basics*, John Wiley & Sons, New York, 1986.

21. R. L. Barbour, H. L. Graber, R. Aronson, J. Lubowsky, "Determination of macroscopic optical properties of multilayer random media by remote sensing," *Time-Resolved Spectroscopy and Imaging of Tissues*, SPIE vol. 1431, pp. 52-62, 1991.

22. H. L. Graber, R. L. Barbour, J. Lubowsky, R. Aronson, B. B. Das, K. M. Yoo, R. R. Alfano, "Evaluation of steady-state, time- and frequency-domain data for the problem of optical diffusion tomography," *Physiological Monitoring and Early Detection Diagnostic Methods*, SPIE vol. 1641, pp. 6-20, 1992.

23. R. F. Bonner, R. Nossal, S. Havlin, G. H. Weiss, "Model for photon migration in turbid biological media," J. Opt. Soc. Am. A, vol. 4, pp. 423-432, 1987.

24. G. H. Weiss, R. Nossal, R. F. Bonner, "Statistics of penetration depth of photons re-emitted from irradiated tissue," J. Modern Optics, vol. 36, pp. 349-359, 1989.

25. R. Aronson, unpublished data.

26. M. Williams, "The relation between various contributons; variable used in special theory," Nucl. Sci. Eng., vol. 63, pp. 220- , 1977.

27. A. Dubi, S. A. W. Gerstl, D. Dudziak, "Monte Carlo aspects of contributons," Nucl. Sci. Eng., vol. 68, pp. 19- , 1978.

28. R. L. Barbour, H. L. Graber, Y. Wang, J. Chang, R. Aronson, "A perturbation approach for optical diffusion tomography using continuous-wave and time-resolved data," accompanying paper.

29. S. R. Arridge, P. van der Zee, M. Cope, D. Delpy, "New results for the development of infra-red absorption imaging," *Biomedical Image Processing*, SPIE vol. 1245, pp. 93-102, 1990.

30. S. R. Arridge, P. van der Zee, M. Cope, D. Delpy, "Reconstruction methods for infra-red absorption imaging," *Time-Resolved Spectroscopy and Imaging of Tissues*, SPIE vol. 1431, pp. 204-215, 1991.

31. R. R. Alfano, private communication.

32. M. A. O'Leary, D. A. Boas, B. Chance, A. G. Yodh, "Refraction of diffuse photon density waves," Phys. Rev. Lett., vol. 69, pp. 2658-2661, 1992.

33. M. V. Klibanov, J. Malinsky, "Newton-Kantorovich method for three-dimensional potential inverse scattering problem and stability of the hyperbolic Cauchy problem with time-dependent data," Inverse Problems, vol. 7, pp. 577-596, 1991.

34. M. V. Klibanov, F. Santosa, "A computational quasi-reversibility method for Cauchy problems for Laplace's equation," SIAM J. Applied Math., vol. 51, pp. 1653-1675, 1991.